Colloidal suspensions in one-phase mixed solvents under shear flow

Armand Barbot, Takeaki Araki

Colloidal suspensions in one-phase mixed solvents under shear flow

Armand Barbot[a,b] **and Takeaki Araki**[*] [a,c]

We numerically studied the behaviour of colloidal suspensions in one-phase binary liquid mixtures under shear flows. Far from the phase-separation point, the colloidal particles are well dispersed and the suspension exhibits a Newtonian viscosity. When the mixture is close to the coexistence curve, the colloidal particles aggregate by attractive interactions due to the concentration heterogeneity caused by surface wetting, and the viscosity of the suspension increases. Near the phase-separation point, the viscosity increases when the fraction of species favoured by the surface of a colloid particle is small. The mixture also exhibits shear thinning behaviour, since the aggregated structure is rearranged into small clusters due to the shear flow. Our simulations indicate that the concentration profile around each particle is not significantly disturbed by the shear flow at the onset of the structural rearrangements. The effective interaction is independent of the shear flow and remains isotropic.

1 Introduction

Suspensions of attractive colloidal particles exhibit various rheological properties, which depend on the particle concentration, the inter-particle interactions and the resultant microstructures.[1–18] When the particle concentration is dilute and the inter-particle interactions are negligible, the suspension behaves as a viscous liquid obeying the Einstein viscosity equation.[1] If the particle concentration is increased and/or the interactions are strengthened, the particles become aggregated. They often form a fractal pattern, depending on the kinetic process of the aggregation.[19] The expanded structure of the fractal pattern may increase the suspension viscosity.[4–12] Furthermore, if the particles percolate and/or are jammed, the suspension exhibits a solid-like behaviour as a gel[13–17] or a glass.[3,18]

The aggregated pattern depends on the properties of the attractive interaction, *e.g.*, its strength, its range and whether the contact is sticky. One of the well-established methods for controlling inter-particle interaction is based on the DLVO theory,[20,21] which describes the interplay between the van der Waals and electrostatic interactions. In a salt-free solvent, a suspension of charged particles is stablised against the aggregation because of the electrostatic repulsive interactions. Adding a sufficiently large amount of salt screens the electrostatic interaction and causes the particles to aggregate. It is also known that non-adsorbing polymers can induce attractive interactions among colloidal particles.[22,23] In the vicinity of a particle surface, the polymer chains are expelled because of steric interactions. The imbalance of the osmotic pressure between the polymer-depleted zone and the bulk liquid pushes particles against each other. The strength and range of this effect can be tuned by changing the concentration and the gyration radii of the polymers.[24]

[a] *Department of Physics, Kyoto University, Sakyo-ku, Kyoto 606-8502, Japan.* [b] *École Normale Supérieure Paris Saclay, 61, avenue du Président Wilson 94235 Cachan cedex, France.* [c] *CREST, JST, Honcho 4-1-8, Kawaguchi-shi, Saitama 332-0012, Japan. E-mail: araki@scphys.kyoto-u.ac.jp*

Binary liquid mixtures also are useful for inducing attractive interactions among particles.[20,25–53] In a phase-separated mixture, the contact angle between the two phases on the particle surface is determined using the Young's equation.[20,27]. If one of the separated phases has a sufficiently higher affinity for the surface than the other phase, the preferred phase wets the particle surfaces completely. When the layers covering the different particles overlap, an attractive interaction is induced between the particles.[20,25–28] This interaction is called a capillary bridging force, and it is well known for particles in a gas-liquid coexistence state of a one-component liquid.[54,55]. The strength and range of the interaction are determined by the relative fraction of the preferred phase. It has been reported experimentally that the capillary forces can give rise to elastic or gel-like rheological properties.[29–31]

On the other hand, when both phases have an equal or nearly equal affinity for the particle surface, the particles tend to gather at the interfaces between the separated phases.[32,33] The particles play the role of surfactants and stabilise the phase-separation pattern, as in emulsions. The stabilised mixture is called a Pickering emulsion.[34] When both phases have nearly the same volume fractions, the emulsion forms bicontinuous patterns. When the particles are jammed at the interfaces, the suspension behaves as a solid.[35–37]

Even for binary mixtures in a one-phase state, attractive interactions are induced among particles when the particle surface prefers one of the mixture components.[26,28,38–42,56,57] Because of wetting between the particles and the binary solvent, the concentration of the favoured species is enriched near the surfaces. Near the phase-separation point, the wetting interaction can induce the phase-separation at the surface.[58,59] When the heterogeneous profiles of the concentration field overlap, an attractive interaction occurs between the particles, which is so strong that it leads to aggregation of the colloidal particles.[43–50,60] This interaction is called a critical Casimir effect or adsorption-induced interaction. In this article, we use it with the latter term.

Although the static properties of the adsorption-induced in-

teractions in colloidal systems have been studied well recently, their dynamic behaviour is still not fully understood. In this article, we numerically investigate the rheological properties of colloidal suspensions in binary mixture solvents. In particular, we focus on those in one-phase mixed states, where the adsorption-induced interaction occurs between the particles. This adsorption-induced interaction can be controlled easily by changing the temperature, and it is reversible. Thus, this interaction can be used to tune the rheological properties of the colloidal suspension. Although one can easily change the interactions among particles and the resultant aggregated structures by adding salts or additives such as polymers, it is not easy to tune the interaction reversibly. It is quite difficult to remove such additives once they have been dissolved.

2 Numerical Model

2.1 Free energy functional

First, we consider the free energy of a binary liquid mixture containing spherical particles. Several simulation methods for studying such mixtures have been developed.[36,44,62–66] The simulation model in this article is basically the same as that used in our previous studies.[67,68]

We denote the solvent species with higher affinity for the particle surface as 'A', and the other one as 'B'. The volume fractions of the solvents A and B are given by ϕ and $1-\phi$, respectively. We describe particles with a smooth shape function as[16,17,51,67–70]

$$\psi_i(\mathbf{r}) = \frac{1}{2}\left\{\tanh\left(\frac{a-|\mathbf{r}-\mathbf{R}_i|}{d}\right)+1\right\}. \tag{1}$$

Here $\mathbf{r}$ is the coordinate in a three-dimensional lattice space, and $\mathbf{R}_i$ is the position of the i-th particle in an off-lattice space. The parameter a is the radius of the particle, and d represents the width of the smooth interface. We respectively define the particle and surface distribution functions as

$$\psi(\mathbf{r}) = \sum_i \psi_i(\mathbf{r}) \tag{2}$$

and

$$\psi_s(\mathbf{r}) = d\sum_i |\nabla\psi_i|. \tag{3}$$

$\psi(\mathbf{r})$ represents the particle distribution. In the limit $d\to 0$, position $\mathbf{r}$ is inside one of the particles when $\psi(\mathbf{r})=1$, while $\mathbf{r}$ is in the solvent when $\psi(\mathbf{r})=0$. Its spatial average $\langle\psi\rangle$ gives the particle volume fraction. Also, in the same limit, $|\nabla\psi_i|$ behaves as $\delta(|\mathbf{r}-\mathbf{R}_i|-a)$ in eqn (3). Finally, ψ_s gives the particle surface distribution.

The free energy functional consists of three parts:

$$\mathscr{F} = \mathscr{F}_m + \mathscr{F}_w + \mathscr{F}_p. \tag{4}$$

The first term is the mixing free energy given by[71]

$$\mathscr{F}_m = \frac{T}{v_0}\int d\mathbf{r}(1-\psi)\left\{f(\phi)+\frac{C}{2}|\nabla\phi|^2\right\}, \tag{5}$$

where T is the temperature and the Boltzmann constant is set as unity. v_0 is the molecular volume and C is the coefficient of the gradient term, related to the interfacial tension; it is of the order of $v_0^{2/3}$. $f(\phi)$ is the bulk mixing free energy, which is given by

$$f(\phi) = \phi\ln\phi + (1-\phi)\ln(1-\phi) + \chi\phi(1-\phi), \tag{6}$$

where χ is the interaction parameter between the two fluid components. Using mean-field approximation, the coexistence curve is given by

$$\chi_{cx}(\langle\phi\rangle) = \{\ln\langle\phi\rangle - \ln(1-\langle\phi\rangle)\}/(2\langle\phi\rangle-1), \tag{7}$$

where $\langle\phi\rangle$ is the average concentration. $\chi=2$ and $\langle\phi\rangle=1/2$ correspond to the critical point of the phase-separation. Also, the distance from the phase boundary is given by $\chi_{cx}-\chi$. The mean-field correlation length is $\xi = d|1/\langle\phi\rangle + 1/(1-\langle\phi\rangle) - 2\chi|^{-1/2}$. It diverges at the spinodal point $\chi_{sp} = \{1/\langle\phi\rangle + 1/(1-\langle\phi\rangle)\}/2$, which is larger than χ_{cx} for off-critical mixtures ($\langle\phi\rangle\neq 1/2$). Furthermore, the correlation length does not diverge on the coexistence curve when $\langle\phi\rangle\neq 1/2$. We confirmed that the solvent is phase-separated when $\chi>\chi_{cx}$ in our simulation without the particles. However, we note that χ_{cx} does not give the correct phase-separation point in mixtures containing particles. The wetting interaction promotes the local phase-separation in the vicinity of the particles, and the average concentration is effectively changed because of the depletion effect. We will see these effects below.

The second term in eqn (4) describes the interplay between the concentration field and the particles.[58,59] It is given by[67,68,70]

$$\mathscr{F}_w = -\frac{T}{v_0}\int d\mathbf{r}\left\{W\psi_s(\phi-\phi_p) + \frac{\chi_p}{2}\psi(\phi-\phi_p)^2\right\}, \tag{8}$$

where the first term on the right hand side is the wetting interaction between the particle surface and the mixture solvent, and W is the strength of the wetting interaction. When the value of W is positive, the particle surface favours the A-species. We artificially introduced the second term to prevent the liquid from penetrating into the particles, and χ_p and ϕ_p are its control parameters. Without this term, the concentration field ϕ inside the particles influences the wetting behavior. We confirmed that the choice of χ_p does not change our results if χ_p is sufficiently large.

The third term in eqn (4) represents direct interaction among the particles and is given by

$$\mathscr{F}_p = \sum_{i<j} U(R_{ij}), \tag{9}$$

where $R_{ij} = |\mathbf{R}_i - \mathbf{R}_j|$ is the distance between the centres of the mass of the i- and j-th particles, and $U(R)$ is a pairwise potential. In this study, we employ the repulsive part of the Lennard-Jones potential. $U(R) = 4U_0\{(\sigma/R)^{12} - (\sigma/R)^6\} + U_0$ for $R < 2^{1/6}\sigma$ and $U(R) = 0$ for $r \geq 2^{1/6}\sigma$, where we set $\sigma = 2a + d$. $\mathscr{F}_\mathrm{p}$ avoids overlaps between particles.

2.2 Time development equations

Next, we consider the hydrodynamic flow of a binary mixture with colloidal particles under shear flow. Even in the absence of particles, it is known that shear flow influences the critical phenomena[71,72] and the phase-separation pattern.[73–75] Also, the resultant interfacial structure changes the rheological properties of the binary mixture.[76]

In our geometry, the hydrodynamic flow is given by

$$\mathbf{v} = \mathbf{u} + \dot{\gamma}(z - z_0)\mathbf{e}_x, \tag{10}$$

where the x, y and z axes are the flow, the vorticity and the shear directions respectively. $\dot{\gamma}$ is the shear rate and $z = z_0$ is the zero-shear plane. $\mathbf{e}_\alpha$ is a unit vector along the α-axis. Hereafter, α and β represent x, y and z, and we sum over repeated indices. $\mathbf{u}$ represents the deviation of the flow field from the applied shear flow. Neglecting non-linear terms, the hydrodynamic equation for $\mathbf{u}$ is given by

$$\rho \frac{\partial u_\alpha}{\partial t} = -\dot{\gamma}(z - z_0)\nabla_x u_\alpha + f_\alpha - \nabla_\alpha p + \nabla_\beta \Sigma^\mathrm{v}_{\alpha\beta}, \tag{11}$$

where ρ is the mass density, which we assume to be the same for all the components. The first term on the right hand side of eqn (11) corresponds to the convection due to the applied shear flow. p is a part of pressure, which is determined by the incompressible condition $\nabla \cdot \mathbf{u} = 0$. Here, $\Sigma^\mathrm{v}_{\alpha\beta}$ is the viscous stress expressed by

$$\Sigma^\mathrm{v}_{\alpha\beta} = \eta(\nabla_\alpha u_\beta + \nabla_\beta u_\alpha) + \eta\dot{\gamma}(\delta_{\alpha z}\delta_{\beta z} + \delta_{\alpha x}\delta_{\beta x}). \tag{12}$$

In the spirit of the fluid particle dynamics method, we assume that the viscosity η depends on the particle distribution as $\eta(\mathbf{r}) = \eta_0 + (\eta_\mathrm{p} - \eta_0)\psi(\mathbf{r})$, where η_0 is the fluid viscosity and η_p is the viscosity inside a particle. In the limit $\eta_\mathrm{p}/\eta_0 \to \infty$, our particles behave as solid objects. The last term in eqn (12) represents the shear stress due to the applied shear. With it, the rotations of particles caused by the shear flow are automatically incorporated. The second term in eqn (11) is the force field acting on the binary fluid.[71] It is given by

$$\mathbf{f}(\mathbf{r}) = -\phi\nabla\frac{\delta\mathscr{F}}{\delta\phi} + \sum_i \left(-\frac{\partial\mathscr{F}}{\partial\mathbf{R}_i} + \mathbf{F}^\mathrm{r}_i\right)\frac{\psi_i(\mathbf{r})}{\Omega_i}, \tag{13}$$

where $\Omega_i = \int \mathrm{d}\mathbf{r}\psi_i(\mathbf{r})$ is the effective volume of the i-th particle. The first term on the right hand side of eqn (13) comes from the inhomogeneity of the concentration field, or the interfacial tension. $\mathbf{F}^\mathrm{r}$ represents the thermal fluctuation acting on the particles and leads to Brownian motion of the particles. We note how to determine the amplitude of $\mathbf{F}^\mathrm{r}$ in Appendix B.

The particles are transported with the flow, and their kinetics are described by

$$\frac{\mathrm{d}}{\mathrm{d}t}\mathbf{R}_i = \frac{1}{\Omega_i}\int \mathrm{d}\mathbf{r}\mathbf{u}(\mathbf{r})\psi_i(\mathbf{r}) + \dot{\gamma}(R_{iz} - z_0)\mathbf{e}_x. \tag{14}$$

The second term represents the transportation caused by the applied shear field.

The time development equation of the concentration field ϕ is given by

$$\frac{\partial\phi}{\partial t} = -\nabla\cdot(\phi\mathbf{u}) - \dot{\gamma}(z - z_0)\nabla_x\phi + \nabla\cdot L(\psi)\nabla\frac{\delta\mathscr{F}}{\delta\phi}, \tag{15}$$

where $L(\psi)$ is the kinetic coefficient. We set $L(\psi) = L_0(1 - \psi)$ to eliminate the flux inside the particles, where L_0 is the kinetic coefficient of the bulk mixture. Without particles, the set of eqn (11) and (15) describes the critical phenomena and phase-separation dynamics in fluid mixtures under shear flow.[71] The effect of the shear flow is characterized by the Deborah number $\mathrm{De} = \dot{\gamma}\tau_\mathrm{d}$.[71] τ_d is the characteristic time for the concentration fluctuations. When particles are contained, $(-\partial\mathscr{F}/\partial\mathbf{R}_i)\psi_i/\Omega_i$ in eqn (13) plays the counterpart of the first term of eqn (14).[70]

In the simulations, we set $v_0 = d^3$, $C = d^2$, $\chi_\mathrm{p} = 10$ and $\phi_\mathrm{p} = 0.5$ in the free energy functional. The particle radius is $a = 4d$, and the wetting parameter is $W = 0.5$, so that the component with larger ϕ (the A-species) tends to wet the particle surface. The strength of the soft-core potential is given by $U_0/T = 5$. The viscosity parameters are $\eta_0 = 0.5\rho L_0/T$ and $\eta_\mathrm{p} = 50\eta_0$.

The space is discretized in units of d, and the time increment is $\Delta t = 0.005t_0$, where $t_0 = d^2 v_0/(L_0 T)$ is a characteristic time for our system. Our method is a hybrid simulation, which treats ϕ and $\mathbf{u}$ in the lattice space, and $\mathbf{R}_i$ in the off-lattice space. Then, the motions of the particles are free from the discretization of the space. The choice of the lattice spacing influences the resolution of our simulations. But, our previous studies and simulations with a similar shape function indicated the usage of d as the lattice spacing is efficient for the computations.[16,17,51,67–70,77] The simulations are conducted in a three dimensional space with Lees–Edwards boundary conditions [see Appendix A]. The sizes of the simulation boxes are $(64d)^3$ for the one or two-particle systems, and $(128d)^3$ for many-particle systems.

In many-particle systems, we impose random noise on the particle motions to thermalize their distribution. In eqn (13), the amplitude of $\mathbf{F}^\mathrm{r}$ is determined to satisfy the fluctuation and dissipation relation [Appendix B]. A shear rate of $\dot{\gamma}t_0 = 0.01$ corresponds to the Péclet number for the particles of

Pe$(=\dot{\gamma}\tau_{\rm p}) \cong 1.05$,[1] where $\tau_{\rm d}$ is the characteristic diffusion time of the Brownian particles.

3 Results and discussions

3.1 Pairwise interactions

First, we consider a particle pair suspended in a binary mixture to study the interactions between them in our model. After the system is annealed at a fixed value of χ with no random noise in $\mathbf{F}^{\rm r}$, the particles and the concentration field reach a final state, in which the particles adhere to each other. Figures 1(a) and (b) show the profiles of the concentration field along the line connecting the particle centres. The average compositions are $\langle\phi\rangle = 0.5$ in (a) and 0.35 in (b). The interaction parameter χ is changed. Here, the particle volume fraction is sufficiently small, $\langle\psi\rangle \cong 2.04\times10^{-3}$, so that we can assume the suspension to be in contact with a reservoir of solvent mixture with concentration $\langle\phi\rangle$. Because of the soft-core potential and the interface with the finite thickness, the particles do not touch completely and there remains the solvent in between them. In both mixtures, the composition near the surface increases and the wetting layers are formed at the surfaces. When the wetting layers are bridged, the capillary force acts between the particles. At $\chi = \chi_{\rm cx}$, the adsorption amount for $\langle\phi\rangle = 0.35$ is larger than that for $\langle\phi\rangle = 0.5$.

In Fig. 1(c), we plot cohesive force $F_{\rm c}$ against to the average concentration $\langle\phi\rangle$, for $\chi = 1.5$ and 2.0. In the final state, the cohesive force $F_{\rm c}$ due to the concentration inhomogeneity is balanced against the repulsive force of the soft-core potential U. Thus, we estimate the cohesive force as

$$F_{\rm c}\left[\equiv -\frac{\partial}{\partial R}(\mathscr{F}_{\rm m}+\mathscr{F}_{\rm w})\right] = \left.\frac{\partial U}{\partial R}\right|_{R=|\mathbf{R}_1-\mathbf{R}_2|}. \qquad (16)$$

We define the sign of $F_{\rm c}$ to be positive when the interaction due to the concentration inhomogeneity is attractive. In Fig. 1(d), we plot the cohesive force as a function of χ for $\langle\phi\rangle = 0.2$, 0.35 and 0.5. Here, only the cohesive forces for $\chi < \chi_{\rm cx}$ are plotted. In the simulations with intermediate values of the wetting parameter, the concentration of the A-species near the surfaces is almost equal to that at the coexistence curve when $\chi \geq \chi_{\rm cx}$. If both particles are contained in a droplet that is much larger than the particle radius, the cohesive force is weakened, and the particles then detach. Thus, the cohesive force cannot be defined by our scheme when $\chi > \chi_{\rm cx}$.

Our simulations reproduce the adsorption-induced interaction occurring between particles. The strength of this interaction is larger for $\chi = 2.0$ than that for $\chi = 1.5$, as shown in Fig. 1(c). For the fixed $\langle\phi\rangle$, the strength increases with χ, as shown in Fig. 1(d). As χ increases, the susceptibility of the concentration field to the adsorption interaction also increases. Hence, the concentration field becomes more heterogeneous

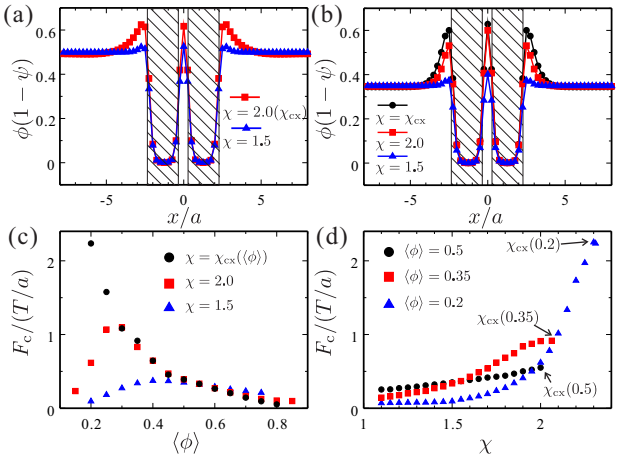

Fig. 1 (a) and (b) The profiles of the concentration field around a particle pair along the line connecting their centres. The average concentrations are $\langle\phi\rangle = 0.5$ in (a) and 0.35 in (b). The interaction parameter is changed. The hatched regions indicate the particles. (c) Plot of the cohesive force between the particles $F_{\rm c}$ as a function of $\langle\phi\rangle$. The interaction parameters are $\chi = \chi_{\rm cx}(\langle\phi\rangle)$, 2.0 and 1.5. (d) Plot of the cohesive force as a function of χ. The average concentrations are $\langle\phi\rangle = 0.5$, 0.35 and 0.2.

near the surfaces as shown in Figs. 1(a) and (b); therefore, the resultant force is strengthened.

Figure 1(c) also shows that the peak position shifts to lower values of $\langle\phi\rangle$ as χ increases. The curve of $F_{\rm c}$ has a broad peak around $\langle\phi\rangle = 0.5$ for $\chi = 1.5$, while it peaks around $\langle\phi\rangle = 0.3$ for $\chi = 2.0$. The behaviour for $\chi = 2.0$ is in accordance with previous studies, which reported that attractive interaction becomes stronger when the component favoured by the particle surface has lower abundance.[25,26,43,47,48,53,57] In Fig. 1(c), we also plot $F_{\rm c}$ on the coexistence curve, $\chi = \chi_{\rm cx}(\langle\phi\rangle)$. The cohesive force increases greatly as $\langle\phi\rangle$ is decreased in our model. In Fig. 1(d), the cohesive force is stronger in the critical mixture with $\langle\phi\rangle = 0.5$ than those in off-critical mixtures for which χ is low. In the A-poor mixtures, on the other hand, the force increases more steeply with increasing χ. Thus, the cohesive force for the A-poor mixtures can be stronger than those for the critical mixture and A-rich mixtures [not shown here]. Hereafter, we consider A-poor mixtures ($\langle\phi\rangle \leq 0.5$), since the adsorption-induced interaction becomes strong for them.

Our preliminary simulations also indicate that the cohesive force is roughly proportional to the particle radius as $F_{\rm c} = Aa$, near the coexistence curve [not shown here]. The coefficient A has the dimension of an interfacial tension and depends on $\langle\phi\rangle$, χ and W. The details of A will be reported elsewhere.

3.2 Particles under shear flow

We next apply shear flow to the two-particle system. Figure 2 shows the snapshots of the particles under the shear flow with $\dot{\gamma}t_0 = 0.01$ in the xz plane. The relative position between the two particles is $\mathbf{R}_1 - \mathbf{R}_2 = (-5a, 0, a)$ in the initial condition. The background colour represents the local concentration field ϕ. We set the average concentration to $\langle\phi\rangle = 0.2$, for which the cohesive force can be strengthened by a greater extent than that in the critical mixture. For this concentration, the coexistence point is $\chi_{\rm cx} \approx 2.31$. The interaction parameter is set as $\chi = 1.6$ in (a) and 2.3 in (b). The particles are transported by shear flow, and they approach each other. When the interaction parameter is $\chi = 1.6$, the particles pass each other without adhering. Near the coexistence point, on the other hand, the particles adhere to each other when they contact, as shown in Fig. 2(b). After the adhesion, the particle pair exhibits a tumbling motion, the frequency of which depends on the shear rate [see the supplementary movies]. In Fig. 2(b), formation of the adsorption layers on the particle surfaces and bridging between them are observed. In Fig. 2(a), on the other hand, the concentration inhomogeneity is not sufficiently large to induce an interaction that is strong enough to bond the particles against the shear flow.

These behaviours depend on the shear rate. In Fig. 2(c), we plot the threshold shear rate $\dot{\gamma}_{\rm t}$, which separates the adhered state [Fig. 2(b)] and the separated state [Fig. 2(a)], with respect to χ. The threshold shear rate increases with χ and is determined by the balance between the shear force and the cohesive force. This behaviour is reasonable, since the attractive force between the particles increases with χ, as indicated in Fig. 1(d). From dimensional analysis, we expect the threshold shear rate to behave as $\dot{\gamma}_{\rm t} = cA/\eta_0 a$, where c is a numerical factor. This expected shear rate is shown by the broken curve in Fig. 2(c), using the force values plotted in Fig. 1(d) and setting $c = 0.5$. This relation indicates that the threshold shear rate decreases when the particles are large.

3.3 Concentration field around a particle under shear flow

In non-equilibrium conditions under external fields, the effective interaction may be different from that in an equilibrium state, since the concentration field mediating the interactions is disturbed by the external field.[51] To determine the influence of shear flow on the concentration field, we show in Fig. 3 the concentration profiles around a single particle under the shear flow. The profiles along the $(1,0,1)$-, $(1,0,-1)$- and $(0,1,0)$-directions from the particle centre are plotted. The average concentration and the interaction parameter are $\langle\phi\rangle = 0.2$ and $\chi = 2.3$, respectively. The shear rates are $\dot{\gamma}t_0 = 0.004$ in (a) and 0.1 in (b), where the threshold shear rate is estimated as $\dot{\gamma}t_0 \cong 0.035$ from Fig. 2(c). When the shear

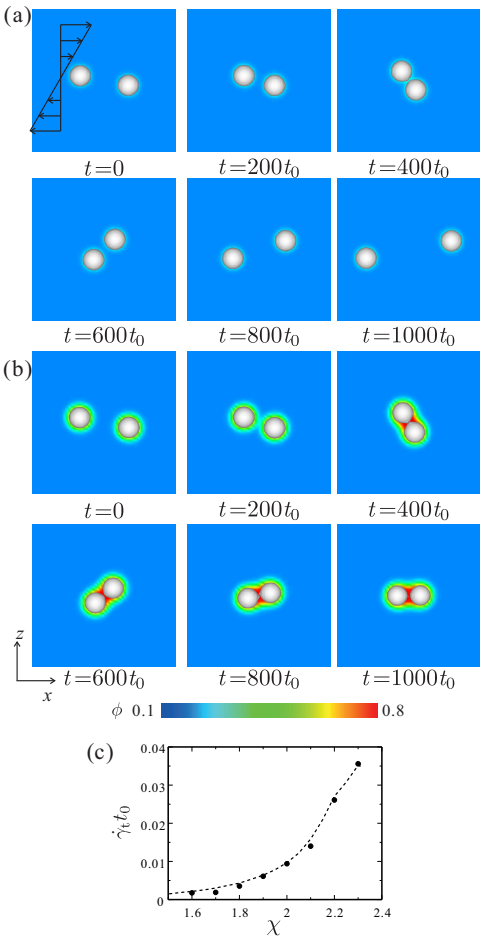

Fig. 2 Snapshot of two particles under a shear flow with $\dot{\gamma}t_0 = 0.01$. The average concentration is $\langle\phi\rangle = 0.2$, and the interaction parameter is $\chi = 1.6$ in (a), and $\chi = 2.3$ in (b). (c) Plot of the threshold shear rate $\dot{\gamma}_{\rm t}$ with respect to χ. The broken curve is given by $cF_{\rm c}/\eta_0 a^2$, using the values of $F_{\rm c}$ shown in Fig. 1(d).

rate is small, the concentration profiles do not depend significantly on the direction. This suggests that the interactions among the particles are not influenced by the shear flow and remain isotropic. As discussed below, aggregated structures are considerably modified in many-particle systems, even under small shear rates. On the other hand, when the shear rate is large, Fig. 3(b) shows that the adsorption layer is elongated along the $(1,0,1)$-direction, whereas it is compressed along the $(1,0,-1)$-direction. The adsorption layer is almost free from the shear flow in the $(0,1,0)$-direction. These differences suggest that the interaction becomes anisotropic under high shear flow, but that the anisotropic part remains small compared to the isotropic part, even for $\dot{\gamma}t_0 = 0.1$.

The concentration pattern in the steady state is determined by the balance between the convective flow and the diffusion flux. It is characterised by the Deborah number $\mathrm{De} = \dot{\gamma}\tau_\mathrm{d}$.[71] From mean-field theory, the characteristic time τ_d for the concentration diffusion is given by $\tau_\mathrm{d} = (\xi/d)^2 t_0$. In off-critical mixtures, the diffusion time does not diverge and remains finite even on the coexistence curve. In the mixture of $\langle\phi\rangle = 0.2$, the diffusion time is estimated as $\tau_\mathrm{d} \cong 0.83t_0$ at $\chi = 2.3$, so that De is much smaller than unity in Fig. 3(a). Also, since the applied shear rates are lower than $1/\tau_\mathrm{d}$, the concentration field can recover an equilibrated pattern via the diffusion process. Since the threshold shear rate is expected to be proportional to $1/a$, the condition of $\dot{\gamma}_\mathrm{t}\tau_\mathrm{d} \ll 1$ is easily satisfied for larger particles.

When $\mathrm{De} \gg 1$, on the other hand, one expects the concentration field to be homogenized, so that the resultant adsorption-induced force becomes smeared out. However, because of numerical instability, we have not conducted simulations with such high shear rates. Near the critical point, the characteristic diffusion time τ_d diverges, which contrasts with the case of an off-critical mixture. Thus, the resultant interaction is expected to be easily modulated by the shear flow in the vicinity of the critical point.

It has been reported that the viscosity of a dilute suspension in a binary mixture changes with the temperature.[61] The shear deformation of the concentration field increases the viscosity. In our simulations, however, this effect is not so important.

3.4 Colloidal suspensions in equilibrium

Next, we consider colloidal suspensions constituting many particles. No shear is applied. The system contains 10^3 particles, and the particle volume fraction is $\langle\psi\rangle \cong 0.128$. Herein, a random force $\mathbf{F}^\mathrm{r}$ has been included to thermalize the particle distributions. [see Appendix B] In our simulations, the Peclet number Pe for the colloid Brownian motion is typically one or two orders magnitude larger than the Deborah number De. Figures 4(a) and (b) show the snapshots of the particles and concentration of the binary mixture at $t = 2000t_0$. The mixture volume fraction is $\langle\phi\rangle = 0.35$, for which the viscosity of the suspension is greatly increased as shown below. The interaction parameter is $\chi = 1.5$ in (a) and $\chi = \chi_\mathrm{cx}$ in (b). In the upper panels, the blue spheres represent the particles and the grey surfaces are the interfaces defined by isosurfaces of $\phi = 0.5$. The middle panels show the concentration fields at the plane $y = 0$.

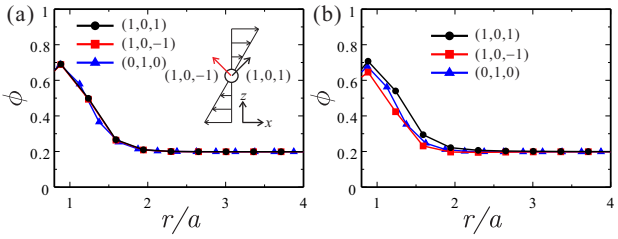

Fig. 3 Profiles of the concentration field ϕ along the $(1,1,0)$-, $(1,-1,0)$- and $(0,0,1)$-directions. The average concentration is $\langle\phi\rangle = 0.2$ and the interaction parameter is $\chi = 2.3$. The shear rate is $\dot{\gamma}t_0 = 0.004$ in (a) and 0.1 in (b).

The particles are well dispersed at $\chi = 1.5$. In the lower panels, we show the radial distribution function $g(r)$ of the particles; it is similar to that of a fluid. A peak is observed near $r = 1.2\sigma$. The peak position is determined by the balance between the adsorption-induced interaction and soft-core potential. Thus, the peak position can be larger than $r = \sigma$. For $r > 2\sigma$, $g(r)$ is almost constant. It indicates there is no long-range order in this suspension. In the case of $\chi = \chi_\mathrm{cx}$, on the other hand, the particles aggregate as shown in Fig. 4(b).[25,43,47,48,50,53] The height of the main peak in $g(r)$ increases and another peak is also formed around $r \cong 2.0\sigma$. These peaks reflect the particle clustering. In the middle panels of Fig. 4(b), we can see domains of the A-rich phase appearing between the particles. These bridging domains bind the particles against the random fluctuations.

Figure 5 shows the histograms of the concentration field $P(\phi)$. To consider the concentration field only outside the particles; it is defined as

$$P(\phi_1) = \frac{\sum_{x,y,z}\{1-\psi(x,y,z)\}\Theta(\Delta\phi - |\phi(x,y,z)-\phi_1|)}{\Delta\phi\sum_{x,y,z}\{1-\psi(x,y,z)\}}, \tag{17}$$

where $\Theta(x)$ is the Heaviside step function and $\Delta\phi = 0.001$. The average concentrations are $\langle\phi\rangle = 0.35$. The colloidal volume fraction is $\langle\psi\rangle = 0.128$ in (a) and 0.033 in (b). Each curve has a large peak on the left hand side and a small one on the right hand side even though the systems are in a one-phase state. The small right hand peak corresponds to the preferential adsorption onto the particle surface. We found that the position of the large left hand peak, which corresponds to the

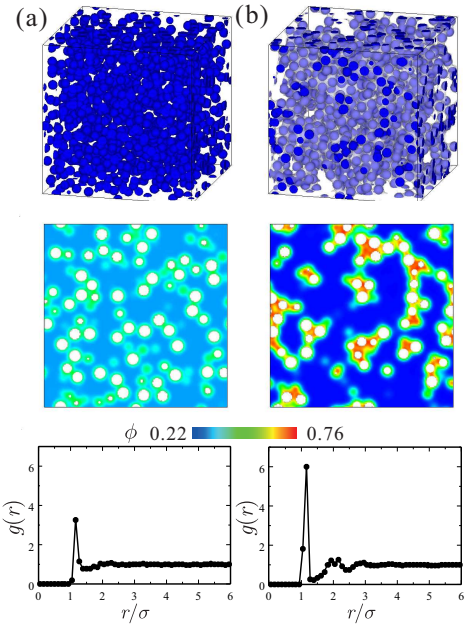

Fig. 4 Snapshots of the particle distributions and the interface structures (upper panels). The interaction parameter is $\chi = 1.5$ in (a) and $\chi = \chi_{cx}$ in (b). The particle volume fraction is $\langle\psi\rangle = 0.128$. The concentration fields are shown in the middle panels. The radial distribution function of the particles for $\chi = 1.5$ and $\chi = \chi_{cx}$ in the lower panels.

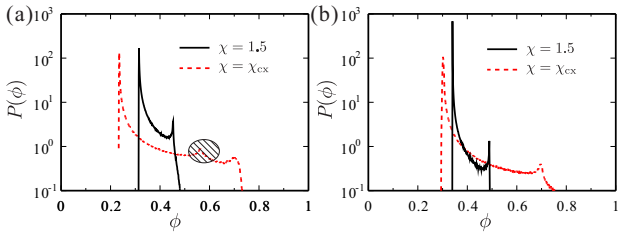

Fig. 5 Histograms of the concentration distribution for $\langle\phi\rangle = 0.35$. The colloidal volume fraction is $\langle\psi\rangle = 0.128$ in (a) and 0.033 in (b). The second peaks for $\chi = \chi_{cx}$ in the hatched region is a numerical artifact due to the phase field model.

solvent concentration, is shifted to lower values of ϕ from the average $\langle\phi\rangle$. In the mixture with $\langle\psi\rangle \cong 0.128$ at $\chi = \chi_{cx}$, the peak position is $\phi \cong 0.23$. In our model, the system is not in contact with a reservoir of the binary mixture with concentration $\langle\phi\rangle$, so the total amount of the A-species is conserved. Thus, this peak shift is due to depletion of the A-component in the mixed solvent. The shift of the peak position increases with χ, since the amount of the A-species adsorbed at the particle surface increases with χ. Because of the decrease of the A-component in the solvent, the effective interactions are increased in the many-particle suspensions, compared to few-particle systems subject to a reservoir mixture with the same concentration $\langle\phi\rangle$.

As indicated in Fig. 5(b), the peak shift also depends on the particle volume fraction. The total area of the particle surface in the suspension is proportional to the particle volume fraction, so that it is reasonable that the shift should increase with $\langle\psi\rangle$. This depletion effect depends on the particle radius. The degree of the depletion is strongly related to the total area of the particle surfaces in the unit volume. Assuming that the thickness of the adsorption layer to be of the order of the correlation length ξ, the total amount of the adsorption in the unit volume can be roughly estimated as $4\pi a^2 \xi n$, where n is the particle number density, $n = \langle\psi\rangle/(4\pi a^3/3)$. Thus, the degree of the depletion is of the order of ξ/a. If the particle size is large enough, the depletion effect will be negligible.

3.5 Colloidal suspensions under shear flow

Next, we apply shear flow to the many-particle suspension at $\chi = \chi_{cx}$ [Fig. 4(b)]. Figures 6(a)-(c) show the snapshots of the particle and the concentration field under shear flow. Under the shear flow, the aggregated structure deforms along the shear direction and is eventually broken into small clusters. We also observed that the clusters are ruptured by the flow and new clusters are formed by coalescences. Under the balance between the formation and breakup of clusters, the system shows a non-equilibrium steady state. [see the supplementary

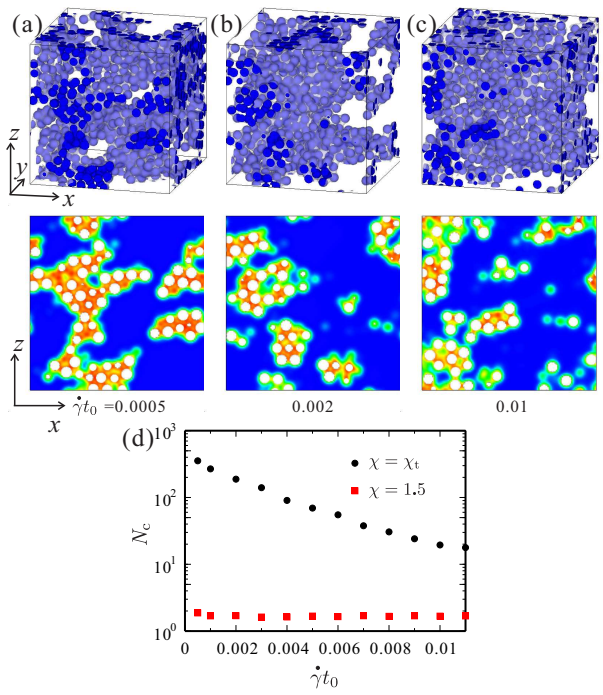

Fig. 6 Snapshots of the particle distribution and the interface structures for $\langle\phi\rangle = 0.35$ and $\chi = \chi_{cx}$. The shear rate is $\dot{\gamma}t_0 = 0.0005$ in (a), 0.002 in (b) and 0.01 in (c). (d) The shear rate dependence of the average cluster size, N_c.

movies.] The clusters tend to be aligned along the shear direction. However, we have not observed a well aligned chain-like aggregated. We considered that the thermal noise suppresses the formation of long chain-like aggregates. Indeed, before the aggregated cluster is enough stretched, it is broken up due to the thermal noise.

The average particle number in the clusters, N_c, is plotted in Fig. 6(d) against the shear rate. We regard the i-th and j-th particles as belonging to the same cluster if their separation is less than a threshold value of $2.5a$, *i.e.*, $R_{ij} < 2.5a$. N_c is given by $N_p/\bar{N}$, where N_p is the total particle number and $\bar{N}$ is the temporal average of the number of the clusters. As the shear rate increases, the cluster size greatly decreases in Fig. 6(d). Our simulations implies that the cluster size decreases exponentially with $\dot{\gamma}$. But we need to collect more data to conclude the dependence of the cluster size on the parameters. For reference, we also plot the average cluster size in the case of $\chi = 1.5$. The average size is about 1.7. The particles are dispersed even when no shear flow is applied as shown in Fig. 4(a), so that N_c for $\chi = 1.5$ is much smaller than that for $\chi = \chi_{cx}$. Also, Fig. 6(d) shows the cluster size is almost independent of the shear rate for $\chi = 1.5$. We have not observed any long-lived clusters. Moreover, for $\chi = 1.5$, the lifetime of such transient clusters is roughly of the order of $\dot{\gamma}^{-1}$. On the other hand, for $\chi = \chi_{cx}$, the clusters are long-lived and the effect of the shear rate on the cluster size becomes significant.

We note that the shear flow of $\dot{\gamma} = \dot{\gamma}_t$ does not correspond to the onset of the rearrangement of the aggregated structure. The threshold shear rate $\dot{\gamma}_t$ in Fig. 2(c) corresponds to the breakup of an adhered particle pair and not breakup of the large aggregates. Even for $\dot{\gamma}$ much smaller than $\dot{\gamma}_t$, the aggregated structures show rearrangements under shear flow. When large shear flow is applied ($\dot{\gamma} > \dot{\gamma}_t$), all the aggregates can be fragmented into single particles. As indicated in Fig. 3, the concentration field around the particles is not disturbed by the shear flow for such small shear rates. At the onset of the rearrangement of the aggregated structure, the adsorption-induced interaction can be regarded as isotropic.

3.6 Rheological properties

It is known that the rheological properties of colloidal suspensions depend on the aggregated structures of the particles. The effective viscosity η_{eff} of the colloidal suspensions in the binary mixtures is plotted in Fig. 7. The average concentration and the particle volume fraction are the same as those in Fig. 6. The numerical scheme for measuring η_{eff} is described in Appendix C. In Fig. 7(a), η_{eff} is plotted against the average concentration $\langle\phi\rangle$. The shear rate is $\dot{\gamma}t_0 = 0.002$. Deep inside the mixing region ($\chi = 1.5$), the viscosity is small and has a broad peak around $\langle\phi\rangle = 0.5$. If χ is increased up to $\chi = 2.0$, the effective viscosity increases and the peak position is shifted to a lower value of $\langle\phi\rangle$. We also plot the effective viscosity on the coexistence curve ($\chi = \chi_{cx}(\langle\phi\rangle)$). There, the effective viscosity is largest around $\langle\phi\rangle = 0.35$, so we chose this concentration in Fig. 4 and below. In Fig. 7(b), the dependences of η_{eff} on χ in both A-poor ($\langle\phi\rangle = 0.35$) and A-rich ($\langle\phi\rangle = 0.65$) mixtures are shown. When χ is small, the effective viscosities are almost the same. This is because the adsorption-induced interactions are too weak to influence the aggregated structures and the viscosity. The viscosities for both mixtures increase as χ increases, but the rate of increase of η_{eff} with χ is larger for the A-poor mixture than that for the A-rich mixture.

Figure 7(c) shows the shear rate dependence of the viscosity for the mixtures with $\langle\phi\rangle = 0.35$. At $\chi = 1.5$, it is shown that the suspension behaves as a Newtonian fluid; the viscosity is independent of the shear rate in the simulated range of $\dot{\gamma}$. We will call this the background viscosity η_b. This is consistent with the observation that the dispersed structure is almost independent of the shear rate as shown in Fig. 6(d). In the one-phase state, far from the coexistence curve, the interactions among the particles are weak enough to make the suspension behave like a suspension of Brownian particles. But, our background viscosity is slightly larger than the viscosity of a hard core suspension, which is about $\eta \approx 1.4\eta_0$ for the same vol-

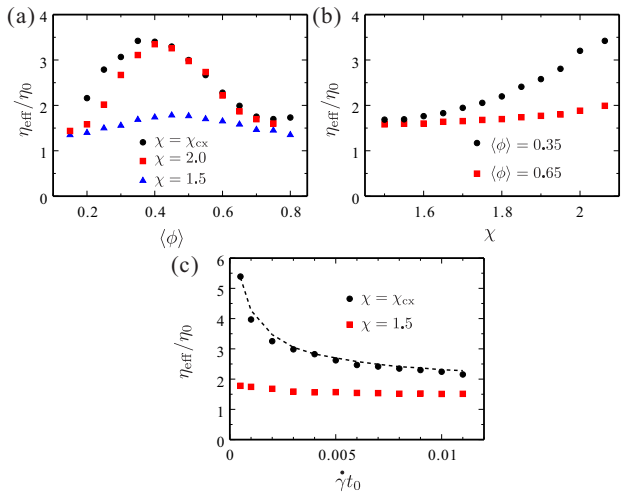

Fig. 7 The effective viscosity as a function of $\langle\phi\rangle$ in (a) and χ in (b). (c) The shear rate dependence of the effective viscosity $\eta_{\rm eff}$. The average concentration is $\langle\phi\rangle = 0.35$ and $\langle\psi\rangle = 0.128$. The broken curve represents $\eta_{\rm eff} - \eta_0 \propto \dot{\gamma}^{-1/2}$.

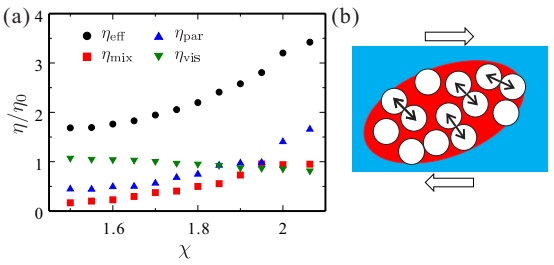

Fig. 8 (a) The strength of each component of the effective viscosity plotted against χ. The details of the viscous components are described in Appendix C. The average concentration and the particle fraction are $\langle\phi\rangle = 0.35$ and $\langle\psi\rangle = 0.128$, respectively. The mixture is at the coexistence curve and under a shear flow of $\dot{\gamma}t_0 = 0.002$. (b) A schematic diagram showing the jamming forces in an aggregate of colloidal particles under shear flow.

ume fraction.[1] We consider that the weak, but finite attractive interactions can form small clusters, as observed in Figs. 4(a) and 6(d), and may increase the suspension viscosity even for $\chi = 1.5$. For the case with $\chi = \chi_{\rm cx}$, the effective viscosity decreases drastically with the shear rate. This is shear-thinning behaviour. At low shear rates, large clusters remain in the quiescent state and do not deform with the shear field. Under high shear rates, the aggregates are fragmented into smaller ones, and the viscosity decreases with $\dot{\gamma}$. Our simulations indicate that the effective viscosity behaves as $\eta_{\rm eff} - \eta_{\rm b} \propto \dot{\gamma}^{-\alpha}$ with $\alpha \cong 1/2$. Similar power law behaviours of the viscosity in suspensions of attractive colloids have been reported.[12] However, its power is given by $\alpha \cong 0.84$, which is larger than the value obtained in this study. The physical origin of our power-law behaviour remains unexplained.

In Fig. 8(a), the effective viscosity $\eta_{\rm eff}$ is divided into three parts. $\eta_{\rm vis}$ is related to the viscous stress including the hydrodynamic interactions among the particles [eqn (12)]. $\eta_{\rm par}$ originates from the direct particle interactions, and $\eta_{\rm mix}$ is related to the mixed solvent. Detailed expressions for these terms are described in Appendix C, and we plot them with respect to χ in Fig. 8. The average concentration is $\langle\phi\rangle = 0.35$, and the particle fraction is $\langle\psi\rangle = 0.128$. The shear rate is $\dot{\gamma}t_0 = 0.002$. Far from the coexistence curve, the viscous stress dominates over the other stress components. The viscous stress is almost constant, although it shows a slight decrease with χ, which may be due to non-linear dependence of the hydrodynamic interaction on the particle concentration. The solvent can flow more easily through channels in the aggregated structure than through a well-dispersed suspension. As χ increases, the other viscosity components increase. In particular, the stress contribution due to the soft-core interactions $\eta_{\rm par}$, increases greatly and exceeds the viscous part. Since the direct soft-core interaction is repulsive, its contribution is generated when an adhered particle pair is compressed along the $(1,0,-1)$-direction by the shear flow (if $\dot{\gamma} > 0$). Near the coexistence curve, most of the particles are aggregated, so the particle stress is enhanced. On the other hand, the cohesive force, which is related to $\eta_{\rm mix}$, is attractive. Thus, it is increased when the aggregated particles are stretched along the $(1,0,1)$-direction by the shear flow (if $\dot{\gamma} > 0$). Our simulations demonstrate that $\eta_{\rm par}$ dominates over $\eta_{\rm mix}$ in this off-critical mixture. As shown schematically in Fig. 8(b), the jamming forces in the colloidal aggregates play a key role in the rheological properties.

4 Summary

In this article, we considered the behaviour of colloidal suspensions in binary mixtures under shear flow. When a suspension is brought close to the phase-separation point of the binary mixture, attractive interactions among the colloidal particles induce particle aggregation. Near a particle surface, the component favoured by the surface is enriched. When the heterogeneous concentration profiles overlap, the attractive interactions occur and they cause the particles to aggregate against the thermal noise. In our simulations, this interaction is strengthened in off-critical mixtures, in which the favoured component has lower abundance.

Under shear flow, the shear force can break the cohesive bonds between the particles and change the aggregated structures. The average size of the aggregated structure decreases with the shear rate. Our simulations indicate that the viscosity of the suspension increases as the suspension approaches the phase-separation point. We also found that suspensions ex-

hibit a shear-thinning behaviour, where the viscosity decreases with the shear rate.

For a particle pair, we obtained the threshold shear rate, which increases as the mixture approaches the coexistence point. At the threshold shear rate, our simulations indicate that the concentration profile around a particle is not significantly disturbed. Thus, the resultant interaction is almost the same as that in quiescent states without shear flow. In the many-particle systems with the random noise, the characteristic particle diffusion time $\tau_{\rm p}$ is one or two order magnitude larger than the diffusion time for the concentration field $\tau_{\rm d}$. The applied shear rate is comparable with $\tau_{\rm p}$, but is larger than $\tau_{\rm d}$. This may indicate that the concentration field can be treated quasistatically and the interaction is described by a potential. But, we consider that solving the concentration field is important even when it is not greatly disturbed by the shear flow. The adsorption-induced interactions do not work among the particles equally, but they depend on the environment around the particles. In a large cluster, as indicated in Fig. 8(b) for example, particles deep inside the large cluster are sometimes surrounded by a sufficient amount of the preferred component. The adsorption-induced interactions are weakened for such particles. On the other hand, strong interactions would work for particles near the boundary of the clusters. This difference may enable us to explain the different power law behaviour of our suspension viscosity from those obtained in the previous simulations with an inter-particle potential. We need to conduct more simulations to obtain the correct viscosity behaviour and clarify its physical mechanism.

The properties of colloidal suspensions are usually controlled by using salt and/or non-adsorbed polymers to change the particle interactions, but such additions are irreversible processes in actual situations. Our studies indicate that rheological properties can be easily tuned by changing the temperature and the fraction of the mixed solvent.

Here we consider a possibility for realizing our findings in actual systems. Phase separation and critical phenomena of mixtures of 2-6 lutidine and water have been intensively studied in experiments. They show a phase diagram with a lower critical point, which is at the 2-6 lutidine mass fraction 0.286 and the temperature $T = 307\,\mathrm{K}$.[43,47,78] The mixture diffusion constant $D(= LT/v_0)$ and the viscosity η near the critical point were obtained as $D = 1.0\times10^{-10}\,\mathrm{m}^2/\mathrm{s}$ and $\eta = 2.1\,\mathrm{mPa\cdot s}$, respectively.[78] Beysens and coworkers studied the aggregation of silica spheres of the diameter 80 nm in these mixture.[43,47] Hence, this mixed solvent is one of the candidate systems for verifying our results. However, our simulations have treated only small particles and shear flow of large shear rates, because of the computational costs. Assuming the average molecular size is $d = 0.6\,\mathrm{nm}$, the particle in our simulations corresponds to a sphere of the diameter 4.8 nm and the wettability $WT = 6\,\mathrm{mN/m}$. The time unit t_0 is 3.6 ns. Then, the shear flow of $\dot\gamma t_0 = 0.001$ corresponds to $2.8\times10^5\,\mathrm{s}^{-1}$, which sounds so large that it might be not easy to set up experiments, which can be compared with our simulations. However, we consider our results can be applied to suspensions of much larger particles, although they will not coincide with experimental observations quantitatively. With larger particles, the shear rate for the rearrangement of the aggregation structure will decrease greatly. We hope that our findings will inspire future experimental studies.

Our simulation method contains several parameters; for simplicity, we fixed most of them In particular, the adsorption-induced interactions and the resultant flow behaviours depend upon the particle radius. Simulations with other particle radii are also thus desired. The wetting parameter W is also important. When we set $W = 0$, our simulation method can be applied to Pickering emulsions, in which we also are interested.

In this article, we considered only the one-phase state of a binary mixture. The rheological properties of phase-separated solvents are also fascinating. In a two-phase state, the phase-separated domains are deformed more easily by shear flow. The deformation of the domains is characterised by hydrodynamic flow induced by the interface tension. In the absence of particles, it is known that phase-separated mixtures show a steady string-like patterns.[73] It will be interesting to see how particles influence the steady state domain patterns and their rheological properties. We hope to report on a series of such studies in the near future.

Acknowledgements

This work was supported by KAKENHI (Grants No. 25000002, No. 24540433 and No. 17K05612), Bridgestone Corporation and CREST, JST (JPMJCR1424). This work was partly supported by the ARPE grant of the ENS Paris-Saclay. Computation was done using the facilities of the Supercomputer Center, the Institute for Solid State Physics, the University of Tokyo and Institute of Chemical Research, Kyoto University.

A Numerical scheme

We solve the concentration ϕ and flow field $\mathbf{u}$ in a three-dimensional lattice space (m,n,ℓ), while the particle positions are defined in off-lattice space. In this study, the lattice space is discretized in units of d. The simulation box size is $L_x\times L_y\times L_z$, where $L_\alpha = dN_\alpha$ and N_α is an integer. To treat the applied shear flow $\dot\gamma z\mathbf{e}_x$, we employed the Lees-Edwards boundary condition. For instance, the boundary condition for ϕ is given by

$$\phi(\mathbf{r}\pm L_z\mathbf{e}_z,t) = \phi(\mathbf{r}\mp\gamma L_z\mathbf{e}_x,t), \tag{18}$$

where $\gamma = \int^t dt' \dot{\gamma}(t')$ is the shear strain. If γL_z is not an integer, we do not have $\phi(\mathbf{r} \mp \gamma L_z \mathbf{e}_z)$ in the lattice space. Then, we approximate it as

$$\begin{aligned} \phi(m,n,\ell) &= \phi(m-\gamma L_z, n, \ell - N_z) \\ &\approx (1-\gamma L_z + [\gamma L_z])\phi(m-[\gamma L_z], n, \ell - N_z) \\ &+ (\gamma L_z - [\gamma L_z])\phi(m-[\gamma L_z]-1, n, \ell - N_z). \end{aligned} \tag{19}$$

Here $[X]$ means the largest integer number smaller than X.

The hydrodynamic flow $\mathbf{u}$ is solved with the Maker and Cell method. The time increment is $\Delta t = 5 \times 10^{-3} t_0$ with $t_0 = d^2 T / L_0$. The Reynolds number in the colloidal systems is very small. In order to weaken the effect of inertia, we develop the hydrodynamic flow without updating ϕ and $\{\mathbf{R}_i\}$ until $\int d\mathbf{r} |\rho \partial \mathbf{u}/\partial t|^2 / \int d\mathbf{r} |\mathbf{f}|^2$ becomes smaller than some small value h. In this study, we use $h = 10^{-2}$. The time evolution of the concentration field and the particle positions are solved using an explicit Euler scheme.

B Random noise

In order to thermalize the many-particle systems, we impose random forces for the particles. Here we describe how to determine the amplitude of the random force.

First, we impose a constant force $\mathbf{F}_0$ to each particle. The particles move along the force on average and the average particle velocity $\langle \mathbf{V} \rangle$ is obtained. We confirmed that the average velocity is almost proportional to the force magnitude, so that we obtain a frictional constant as $\zeta = |\mathbf{F}_0| / |\langle \mathbf{V} \rangle|$. The frictional constant increases as the particle volume fraction $\langle \psi \rangle$ increases.

Then, we impose random forces with an arbitrary magnitude $\tilde{\mathbf{F}}_i^{\mathrm{r}}$ to the particles with no constant force. The particles show the Brownian motions and a diffusion constant $\tilde{D}$ is obtained. The diffusion constant is proportional to the mean square of the random force as $\tilde{D} = k \langle |\tilde{\mathbf{F}}_i^{\mathrm{r}}|^2 \rangle$, then we obtain the coefficient k. The fluctuation and dissipation theorem gives the diffusion constant as $D = 6T/\zeta$. Thus, we can determine the strength of the random force for a target temperature T as $\langle |\mathbf{F}_i^{\mathrm{r}}|^2 \rangle = 6T/(k\zeta)$.

C Mechanical stress

In order to study the rheological properties of binary fluids under shear flow, we must measure the shear stress. In our system, the shear stress constitutes four parts.

$$\Sigma_{\alpha\beta} = \Sigma^{\mathrm{m}}_{\alpha\beta} + \Sigma^{\mathrm{w}}_{\alpha\beta} + \Sigma^{\mathrm{p}}_{\alpha\beta} - \Sigma^{\mathrm{v}}_{\alpha\beta}, \tag{20}$$

where $\Sigma^{\mathrm{v}}_{\alpha\beta}$ is the viscous stress defined by eqn (12).

$\Sigma^{\mathrm{p}}_{\alpha\beta}$ is the stress due to the direct interactions among the particles. Its spatial average is given by

$$\langle \Sigma^{\mathrm{p}}_{\alpha\beta} \rangle = \frac{1}{V} \int d\mathbf{r} \Sigma^{\mathrm{p}}_{\alpha\beta} = \frac{1}{V} \sum_{i<j} (\mathbf{R}_i - \mathbf{R}_j)_\alpha \mathbf{F}_{ij\beta} \tag{21}$$

when $U_{\mathrm{sp}} = 0$. Here $\mathbf{F}_{ij} = -\partial U(|\mathbf{R}_i - \mathbf{R}_j|)/\partial \mathbf{R}_j$ is the force acting the i-th particle from the j-th one, and V is the system volume. We note that

$$\sum_i \int d\mathbf{r} r_\alpha \frac{\psi_i(r)}{\Omega_i} F_{i\beta} = \sum_{i<j} (R_{i\alpha} - R_{j\beta}) F_{ij\beta}, \tag{22}$$

where $\mathbf{F}_i = \sum_j \mathbf{F}_{ij}$. $\langle X \rangle$ indicates the spatial average of a variable X.

$\Sigma^{\mathrm{m}}_{\alpha\beta}$ and $\Sigma^{\mathrm{w}}_{\alpha\beta}$ are the stresses stemming from $\mathscr{F}_{\mathrm{m}}$ and $\mathscr{F}_{\mathrm{w}}$, respectively. If the particles are not included, Σ_{m} is calculated as[71]

$$\begin{aligned} \frac{\nu_0 \Sigma^{\mathrm{m}}_{\alpha\beta}}{T} &= \delta_{\alpha\beta} \left(\phi \frac{\partial f}{\partial \phi} - f - \frac{C}{2} |\nabla \phi|^2 - C\phi \nabla^2 \phi \right) \\ &+ C \nabla_\alpha \phi \nabla_\beta \phi. \end{aligned} \tag{23}$$

Note that this form cannot be directly employed when the mixture contains the particles.

Assuming a small affine transformation $\mathbf{r}' = \mathbf{r} + \Delta\gamma z \mathbf{e}_x$, therefore, we estimate the mechanical stresses as

$$\Sigma^k_{zx} = \frac{\mathscr{F}_k\{\phi', \mathbf{R}_i'; \Delta\gamma\} - \mathscr{F}_k\{\phi, \mathbf{R}_i; \Delta\gamma = 0\}}{\Delta\gamma V}, \tag{24}$$

where $k = \mathrm{m}$ or w. Its spatial average is denoted by $\langle \Sigma^k_{zx} \rangle$. ϕ' and $\mathbf{R}_i'$ are given in the affine transformation as

$$\phi'(\mathbf{r}) = \phi(\mathbf{r}) - (\nabla_x \phi) \Delta\gamma z, \tag{25}$$

$$\mathbf{R}_i' = \mathbf{R}_i + \Delta\gamma R_{iz} \mathbf{e}_x. \tag{26}$$

In calculating these parameters in the main text, we employ $\Delta\gamma = 0.01$.

In Fig. 8, we plot the viscosity due to the concentration $\eta_{\mathrm{mix}} = \langle \Sigma^{\mathrm{m}}_{zx} + \Sigma^{\mathrm{w}}_{zx} \rangle / \dot{\gamma}$, the hydrodynamic viscosity $\eta_{\mathrm{vis}} = \langle \Sigma^{\mathrm{v}}_{zx} \rangle / \dot{\gamma}$, and that due to direct particle interactions $\eta_{\mathrm{par}} = \langle \Sigma^{\mathrm{p}}_{zx} \rangle / \dot{\gamma}$, with $\eta_{\mathrm{eff}} = \eta_{\mathrm{mix}} + \eta_{\mathrm{par}} + \eta_{\mathrm{vis}}$. In the main text, the viscosities are averaged over the time period of $2 \times 10^3 t_0$.

References

1 J. Mewis and N. J. Wagner, *Colloidal Suspension Rheology*, Cambridge University Press, Cambridge, 2012.

2 W. B. Russel, J. Rheol., 1980, **24**, 287-317.

3 V. Trappe, V. Prasad, L. Cipelletti, P. N. Segre, and D. A. Weitz, Nature, 2001, **411**, 772-775.

4 R. Buscall, I. J. Mcgowan, P. D. A. Mills, R. F. Stewart, D. Sutton, L. R. White and G. E. Yates, J. Non-Newt. Fluid. Mech., 1987, **24**, 183-202.

5 M. Chen and W. B. Russel, J. Colloid Interface Sci., 1991, **141**, 564-577.

6 R. Buscall, J. I. McGowan, and A. J Morton-Jones, J. Rheol., 1993, **37**, 621-641.

7 C. Allain, M. Cloitre, and M. Wafra, Phys. Rev. Lett., 1995, **74**, 1478-1481.

8 C. J. Rueb and C. F. Zukoski, J. Rheol., 1998, **42**, 1451-1476.

9 L. Krishnamurthy and N. J. Wagner, J. Rheol., 2005, **49**, 475-499.

10 R. C. Sonntag and W. B. Russel, J. Colloid Interface Sci., 1986, **113**, 399-413.

11 R. C. Sonntag and W. B. Russel, J. Colloid Interface Sci., 1986, **115**, 378-389.

12 L. E. Silbert, J. R. Melrose, and R. C. Ball, J. Rheol., 1999, **43**, 673-700.

13 M. C. Grant and W. B. Russel, Phys. Rev. E, 1993, **47**, 2606-2614.

14 P. J. Lu, E. Zaccarelli, F. Ciulla, A. B. Schofield, F. Sciortino, and D. A. Weitz, Nature, 2008, **453**, 499-503.

15 E. Zaccarelli, J. Phys.: Condens. Matter, 2007, **19**, 323101.

16 H. Tanaka and T. Araki, Europhys. Lett., 2007, **79**, 58003.

17 A. Furukawa and H. Tanaka, Phys. Rev. Lett., 2010, **104**, 245702.

18 K. N. Pham, A. M. Puertas, J. Bergenholtz, S. U. Egelhaaf, A. Moussaïd, P. N. Pusey, A. B. Schofield, M. E. Cates, M. Fuchs, and W. C. K. Poon, Science, 2002, **296**, 104-106.

19 D. A. Weitz and M. Oliveria, Phys. Rev. Lett., 1984, **52**, 1433-1436.

20 J. Israelachvili, *Intermolecular & Surface Forces*, Academic Press, London, 1985.

21 R. J. Hunter, *Foundations of Colloid Science*, Oxford University Press, Oxford, 2001.

22 S. Asakura and F. Oosawa, J. Chem. Phys., 1954, **22**, 1255-1256.

23 W. C. K. Poon, J. Phys.: Condens. Matter, 2002, **14**, R859-R880.

24 S. L. Taylor, R. Evans, and C. P. Royall, J. Phys. Condens. Matter, 2012, **24**, 464128.

25 P. Hopkins, A. J. Archer, and R. Evans, J. Chem. Phys., 2009, **131**, 124704.

26 R. Okamoto and A. Onuki, Phys. Rev. E, 2013, **88**, 022309.

27 H.-J. Butt and M. Kappl, Adv. Colloid Interf. Sci., 2009, **146**, 48-60.

28 S. Yabunaka, R. Okamoto, and A. Onuki, Soft Matter, 2015, **11**, 5738-5747.

29 S. van Kao, L. E. Nielsen, and C. T. Hill, J. Colloid Interface Sci., 1975, **53**, 367-373.

30 E. Koos, and N. Willenbacher, Science, 2011, **311**, 897-900.

31 T. Domenech and S. S. Velankar, Soft Matter, 2015, **11**, 1500-1516.

32 S. U. Pickering, J. Chem. Soc., 1907, **91**, 2001-2021.

33 B. P. Binks and J. H. Clint, Langmuir, 2002, **18**, 1270-1273.

34 R. Aveyard, B. P. Binks, and J. H. Clint, Adv. Colloid Inteface Sci., 2003, **100-102**, 503-546.

35 E. M. Herzig, K. A. White, A. B. Schofield, W. C. K. Poon, and P. S. Clegg, Nature Materials, 2007, **12**, 966-971.

36 K. Stratford, R. Adhikari, I. Pagonabarraga, J.-C. Desplat, M. E. Cates, Science, 2005, **309**, 2198-2201.

37 M. E. Cates and P. S. and Clegg, Soft Matter, 2008, **4**, 2132-2138.

38 M. E. Fisher and P. G. de Gennes, C. R. Acad. Sci. (Paris), Ser. B, 1978, **287**, 207.

39 C. Hertlein, L. Helden, A. Gambassi, S. Dietrich, and C. Bechinger, Nature, 2008, **451**, 172-175.

40 A. Gambassi, A. Maciołek, C. Hertlein, U. Nellen, L. Helden, C. Bechinger, and S. Dietrich, Phys. Rev. E, 2009, **80**, 061143.

41 F. Schlesener, A. Hanke, and S. Dietrich, J. Stat. Phys., 2003, **110**, 981-1013.

42 S. Paladugu, A. Callegari, Y. Tuna, L. Barth, S. Dietrich, A. Gambassi, G. Volpe, Nat. Commun., 2016, **7**, 1038.

43 D. Beysens and D. Esteve, Phys. Rev. Lett., 1985, **54**, 2123-2126.

44 A. C. Balazs, V. V. Ginzburg, F. Qiu, G. W. Peng, and D. Jasnow, J. Phys.: Condens. Matter, 2000, **104**, 3411-3422.

45 H. Löwen, Phys. Rev. Lett., 1995, **74**, 1028-1031.

46 R. R. Netz, Phys. Rev. Lett., 1996, **76**, 3646-3649.

47 B. M. Law, J.-M. Petit, and D. Beysens, Phys. Rev. E, 1998, **57**, 5782-5794.

48 D. Bonn, J. Otwinowski, S. Sacanna, H. Guo, G. H. Wegdam, and P. Schall, Phys. Rev. Lett., 2009, **103**, 156101.

49 V. D. Nguyen, S. Faber, Z. Hu, G. H. Wegdam, and P. Schall, Nat. Commun., 2013, **4**, 1584.

50 N. Tasios, J. R. Edison, R. van Roij, R. Evans, and M. Dijkstra, J. Chem. Phys., 2016, **145**, 084902.

51 A. Furukawa, A. Gambassi, S. Dietrich, and H. Tanaka, Phys. Rev. Lett., 2013, **111**, 055701.

52 H. Tanaka, A. Lovinger, and D. D. Davis, Phys. Rev. Lett., 1994, **72**, 2581-2584.

53 T. F. Mohry, S. Kondrat, A. Maciołek, and S. Dietrich, Soft Matter, 2014, **10**, 5510-5522.

54 C. Bauer, T. Bieker, and S. Dietrich, Phys. Rev. E, 2000,

62, 5324-5338.
55 S. Herminghaus, Adv. Phys., 2005, **54**, 221-261.
56 O. Vasilyev, A. Gambassi, A. Maciołek, and S. Dietrich, Euro. Phys. Lett., 2007, **80**, 60009.
57 R. Okamoto and A. Onuki, J. Chem. Phys., 2012, **136**, 114704.
58 J. W. Cahn, J. Chem. Phys., 1977, **66**, 3667-3672.
59 P. G. de Gennes, Rev. Mod. Phys., 1985, **57**, 827-863.
60 T. F. Mohry, A. Maciołek, and S. Dietrich, J. Chem. Phys., 2012, **136**, 224903.
61 Y. Fujitani, J. Phys. Soc. Jpn., 2014, **83**, 084401.
62 V. V. Ginzburg, P. G. Peng, F. Qiu, D. Jasnow, and A. C. Balazs, Phys. Rev. E, 1999, **60**, 4352-4359.
63 M. Laradji and G. MacNevin, J. Chem. Phys., 2003, **119**, 2275-2283.
64 B. P. Lee, J. F. Douglas, and S. C Glotzer, Phys. Rev. E, 1999, **60**, 5812-5822.
65 Y.-l. Tang and Y.-q. Ma, J. Chem. Phys., 2002, **116**, 7719-7723.
66 D. Suppa, O. Kuksenok, and A. C. Balazs, J. Chem. Phys., 2002, **116**, 6305-6310.
67 T. Araki and H. Tanaka, Phys. Rev. E, 2006, **73**, 061506.
68 T. Araki and H. Tanaka, J. Phys. Condens. Matter, 2008, **20**, 072101.
69 H. Tanaka and T. Araki, Phys. Rev. Lett., 2000, **85**, 1338-1341.
70 T. Araki and S. Fukai, Soft Matter, 2015, **11**, 3470-3479.
71 A. Onuki, *Phase Transition Dynamics*, Cambridge Univ. Press, Cambridge, 2002.
72 A. Onuki, J. Phys.: Condens. Matter, 1997, **9**, 6119-6157.
73 T. Hashimoto, T. Takebe, and S. Suehiro, J. Chem. Phys., 1988, **88**, 5874-5881.
74 C. L. Tucker III and P. Moldenaers, Annu. Rev. Fluid. Mech., 2002, **34**, 177-210.
75 P. Stansell, K. Stratford, J.-C. Desplat, R. Adhikari, and M. E. Cates, Phys. Rev. Lett., 2006, **96**, 085701.
76 M. Doi and T. Ohta, J. Chem. Phys., 1991, **95**, 1242-1248.
77 Y. Nakayama and R. Yamamoto, Phys. Rev. E, 2005, **71**, 036707.
78 J. C. Clunie and J. K. Baird, Phys. Chem. Liq. 1999, **37**, 357-371.